Microbes use encapsulin protein organelles to sequester toxic reactions

Tobias W. Giessen[†,‡] *and Pamela A. Silver**[,†,‡]

Author affiliations:

[†]Department of Systems Biology, Harvard Medical School, Boston, Massachusetts 02115, USA

[‡]Wyss Institute for Biologically Inspired Engineering, Harvard University, Boston, Massachusetts 02115, USA

Corresponding author:

Pamela A. Silver, Harvard Medical School, Department of Systems Biology 200 Longwood Avenue, Warren Alpert Building, Boston, MA 02115, TEL: 617-432-6401, FAX: 617-432-5012, Email: pamela_silver@hms.harvard.edu

Abstract

Cells organize and regulate their metabolism via membrane- or protein-bound organelles. In this way, incompatible processes can be spatially separated and controlled. In prokaryotes, protein-based compartments are used to sequester harmful reactions and store useful compounds. These protein compartments play key roles in various metabolic and ecological processes ranging from iron homeostasis to carbon fixation. We identified more than 900 proteinaceous encapsulin nanocompartment systems in bacterial and archaeal genomes. Encapsulins can be found in 15 bacterial and 2 archaeal phyla. Our analysis reveals 1 new capsid type and 9 previously unknown cargo proteins targeted to the interior of encapsulins. We experimentally characterize 3 newly identified encapsulin systems and illustrate their involvement in iron mineralization, oxidative and nitrosative stress resistance and anaerobic ammonium oxidation, a process responsible for 30% of the N lost from the oceans. We propose that encapsulins represent a widespread strategy for toxic reaction sequestration in prokaryotes.

48 Cells employ compartmentalization to overcome many difficult metabolic and physiological challenges[1].
49 Eukaryotes mainly use membrane-bound organelles to sequester and control the flow of metabolites,
50 store genetic information and segregate protein processing and export[2, 3]. In contrast, the majority of
51 prokaryotes do not possess intracytoplasmic membrane systems and instead rely on alternative
52 approaches to achieve spatial control[4, 5]. A number of different protein-based compartmentalization
53 systems have been discovered, most prominently bacterial microcompartments (BMCs) like the CO_2-
54 fixing carboxysome[6, 7] and ferritins involved in iron homeostasis and maintaining redox balance[8].
55 Encapsulating enzymes or biosynthetic pathways in semi-permeable protein organelles can increase the
56 local concentrations of metabolites and enzymes, prevent the loss of toxic or volatile intermediates [9]
57 and create unique microenvironments necessary for the proper functioning of specialized enzymes [10]. In
58 addition, encapsulation allows for incompatible reactions and processes to take place in a single cell at
59 the same time.

60 A new class of proteinaceous compartments referred to as encapsulin nanocompartments has recently
61 been discovered[11, 12]. They have been reported in a number of bacterial and archaeal genomes and
62 assemble into T = 1 (60 subunits, 20-24 nm) or T = 3 (180 subunits, 30-32 nm) icosahedral hollow
63 capsids. The key feature of encapsulin systems is that they specifically encapsulate cargo proteins, which
64 are targeted to the encapsulin capsid interior via small C-terminal peptide tags referred to as targeting
65 peptides (TPs)[13]. So far, 7 encapsulin systems have been investigated. Encapsulins internalizing ferritin-
66 like proteins (Flps) were discovered in *Thermotoga maritima*[12], *Myxococcus xanthus*[14] and
67 *Rhodospirillum rubrum*[15] while an Flp-encapsulin fusion protein was found in *Pyrococcus furiosus*[16]. The
68 *M. xanthus* encapsulin system is involved in starvation-induced oxidative stress response, protecting
69 cells from the iron-dependent generation of reactive oxygen species (ROS). A second type of encapsulin
70 system encapsulates DyP-type peroxidases (Peroxi) in *Rhodococcus erythropolis*[17], *Brevibacterium*
71 *linens*[18] and *Mycobacterium tuberculosis*[19]. A role in oxidative stress response was proposed based on

72 cargo protein identity. These examples from diverse microbes raise the question of whether
73 compartmentalization using protein-based organelles is much more widespread than previously
74 assumed.

75 Here, we systematically explore the distribution, diversity and function of encapsulin gene clusters in
76 bacterial and archaeal genomes. Our approach is the first comprehensive analysis of encapsulin systems
77 in microbial genomes. By surveying and analyzing the newly identified encapsulin gene clusters, we can
78 assess the potential for functional nanocompartment production in organisms occupying diverse
79 habitats ranging from anaerobic hyperthermophilic environments to the human host, and predict their
80 functions at the molecular level. This enables us to formulate informed hypotheses about the roles
81 encapsulin nanocompartments play in survival, pathogenesis and in shaping global ecological processes.
82 We use a combination of bioinformatics, phylogenetic analysis and biochemistry to reveal and
83 characterize 3 new encapsulation systems involved in key cellular processes - iron mineralization,
84 oxidative and nitrosative stress resistance and anaerobic ammonium oxidation (anammox).

85 **Results**

86 ***Encapsulin systems are widespread in bacteria and archaea***

87 The widespread distribution of encapsulin nanocompartments makes them one of the most
88 predominant classes of protein organelles. Our systematic approach identified 909 encapsulin systems
89 distributed in 15 bacterial and 2 archaeal phyla spanning a remarkable breadth of microbial diversity and
90 habitats. Initially, position-specific iterative (PSI)-BLAST searches using all experimentally confirmed
91 encapsulin capsid proteins were carried out against the NCBI database of non-redundant protein
92 sequences. After consolidating the hits resulting from different searches, the 10 kb up- and downstream
93 regions of the identified encapsulin homologs were searched for the presence of phage-related genes
94 using individual protein BLAST searches. When genes related to any known phage morphotype were

95 detected, hits were excluded from subsequent analysis. This step was necessary to ensure that all
96 identified systems are indeed encapsulins and not unknown HK97-related prophages. This resulted in a
97 list of 909 encapsulins distributed in 15 bacterial and 2 archaeal phyla (Fig. 1A and Supplementary Data
98 1). Encapsulins can be found in anaerobic thermophilic microbes of the genera *Thermotoga*, *Clostridium*
99 (Bacteria) and *Pyrococcus* (Archaea) as well as aerobic mesophilic soil bacteria (e.g. *Streptomyces* and
100 *Bacillus*), cyanobacteria (e.g. *Acaryochloris*) and host-associated microbes, both commensal (e.g.
101 *Bacteroidetes* and *Propionibacterium*) and pathogenic (e.g. *Mycobacterium*, *Escherichia* and
102 *Pseudomonas*). Actinobacteria and Proteobacteria harbor the largest number of encapsulin systems (47
103 and 27%, respectively) while encapsulins can also be found in many less explored phyla like the
104 Planctomycetes and Tectomicrobia. Interestingly, 14 of the identified species contain 2 distinct
105 encapsulin systems (core operons, Data S1). In 8 cases, the systems were of the same core cargo type
106 and likely originated from a duplication of the core operon locus, while in 6 cases, 2 different core cargo
107 types were present (consistently Heme and Peroxi), suggesting independent acquisition via horizontal
108 gene transfer. The presence of multiple encapsulin systems within a single organism argues that each of
109 them conveys a distinct evolutionary benefit.

110 ***A diversity of cargo types***

111 We identify new cargo types and other encapsulin-associated components illustrating that encapsulin
112 systems are more complex than previously assumed. An encapsulin system is defined by the core
113 operon, composed of the encapsulin capsid and core cargo genes (Fig. 1B). All cargo proteins are
114 characterized by the presence of a targeting peptide (TP) at one of the termini. Additional cargo proteins
115 can be located outside the core operon and are referred to as 'secondary cargo'. Other associated
116 components that are not targeted for encapsulation, but might play important functional roles can be
117 encoded close to the encapsulin core operon.

118 Our search reveals 7 previously unknown core cargo types. The set of encapsulin-containing genomes
119 was searched for the presence of core cargo proteins by inspecting the neighborhood of a given
120 encapsulin gene for genes encoding proteins with C- or N-termini similar to known encapsulin TPs using
121 MultiGeneBlast[20]. The 7 newly identified core cargo proteins are generally located directly upstream of a
122 given encapsulin gene (Fig. 1B and C). They include hemerythrins (Heme), di-iron proteins known to
123 coordinate small gaseous compounds like O_2 and NO[21], a new type of 4 helix bundle protein (Geobac)
124 prevalent in Firmicutes and 4 distinct Flp-family proteins[22]. In addition, anammox bacteria of the phylum
125 Planctomycetes, capable of carrying out anaerobic ammonium oxidation[23], exhibit a divergent operon
126 organization with a conserved putative cargo gene located downstream of an unusual fusion-encapsulin.

127 We discovered 4 new secondary cargo proteins and show that up to 4 different cargo types are present
128 in a single genome. One approach to study the physiological functions of encapsulins is to correlate core
129 cargo type with the identity of additional secondary cargo proteins and non-encapsulated genetically
130 associated components[24]. BLAST searches in the set of encapsulin-encoding genomes were carried out
131 using 3 different TP consensus sequences as queries. The first consensus sequence used was based on
132 the TPs of all core cargo types identified in this study. Using the core consensus we identified 76
133 secondary cargo proteins of 4 different types (Flp: 27, Peroxi: 8, Heme: 14 and Ferredoxin (Fer): 27), 3 of
134 them previously unknown (Peroxi, Heme and Fer) (Fig. 2A). Interestingly, the newly discovered
135 Ferredoxins were present exclusively in Geobac-systems found either directly downstream of the
136 encapsulin gene or separated by one other gene. Additionally, TPs present in Ferredoxins were not
137 located at the C-terminus, as is the case for all other identified cargo, but at the N-terminus. Our search
138 using the FolB-based consensus sequence yielded 76 instances of FolB-type secondary cargo proteins
139 and 8 examples of a new putative cargo type, namely BphB (biphenyl dehydrogenase)-like short chain
140 dehydrogenases. Searches using the BfrB-consensus sequence resulted in the identification of 172 BfrB-
141 type secondary cargo proteins. More than one third (363) of all identified systems contain more than

142 one cargo type that is tagged for encapsulation (Supplementary Fig. 1A). We identified 65 instances of 3
143 cargo types being present in one genome and one example of 4 co-occurring cargo proteins (core:
144 Peroxi, secondary: Heme, FolB and BfrB; *Mycobacterium simiae* ATCC 25275). Besides core and
145 secondary cargo, non-targeted associated proteins are often found in the vicinity of encapsulin core
146 operons and are confined to specific genera and core cargo types. They include cupin-type oxygenases
147 found in close association with many Peroxi systems in Mycobacteria (Supplementary Fig. 1B), non-
148 targeted Flp proteins found close to Flp or Flp-fusion systems in archaea (Supplementary Fig. 1C) and
149 different types of electron-transfer proteins clustered around Flp core operons (Supplementary Fig. 1D).

150 The most diverse class of identified cargo are Flp-type proteins. They represent a large superfamily with
151 varied functions unified by the presence of a 4 helix bundle domain harboring a dinuclear iron center[22].
152 A sequence similarity network (SSN) analysis[25] of all (core, fusion and secondary) Flp-type cargo proteins
153 identified in this study allowed us to visualize distinct subfamilies and showed that 7 distinct classes of
154 Flp proteins are targeted for encapsulation by encapsulin compartments (Fig. 2B). Two (Flp-1 and Flp-2)
155 have previously been identified to be part of encapsulin systems either as distinct cargo proteins (*T.*
156 *maritima*, *M. xanthus* and *R. rubrum*)[12, 14, 15] or as an N-terminal fusion domain (*P. furiosus*)[16]. Flp-3,
157 exclusively identified in Archaea, has not been characterized and shows similarity to proteins found in
158 ferric iron- and arsenic-reducing species[26]. Two types of bacterioferritin-like proteins (BfrA and BfrB) are
159 usually involved in maintaining iron homeostasis in various bacteria representing an analogous system
160 to the eukaryotic Ferritins (Ftn)[22]. Additionally, proteins with similarity to DNA-binding proteins from
161 starved cells (DPSL) were identified in a number of archaeal species. Finally, a previously unknown family
162 of double Flp fusion proteins (Flp+Flp) was shown to be present in a number of thermophilic bacteria
163 (Supplementary Fig. 1E).

164 ***Encapsulins can be divided into four families***

165 Encapsulin nanocompartments were known to assemble into either small (ca. 22 nm in diameter) or
166 large (ca. 32 nm in diameter) capsids with triangulation numbers of *T*=1 (60 subunits) or *T*=3 (180
167 subunits), respectively[11]. However, it was unclear what factors determine their assembly into small or
168 large compartments or how capsid size correlates with cargo type and function. To address these issues,
169 we initially carried out a SSN analysis of all identified encapsulin capsid proteins (Fig. 3A). We found that
170 encapsulins cluster into 4 distinct groups (edge % identity: 24). It was immediately apparent that all Flp-
171 fusion encapsulins cluster together. By mapping the characterized systems onto our network we found
172 that small (60mer) encapsulins cluster together in one of the 2 large sequence groups while the single
173 known large (180mer) system (*M. xanthus*) was found in the second large sequence cluster
174 (Supplementary Fig. 2A). None of the known systems mapped onto the fourth sequence cluster from
175 now on referred to as 'New'.

176 There are 2 main determinants at the sequence level predictive of capsid size (Supplementary Fig. 2B). A
177 T3-motif (GPxGxG) present only in large capsids occurs at the N-terminal end of the E-loop while an
178 additional 8 to 10 residue E-loop insertion is present in most *T*=3 capsids. The fourth sequence cluster
179 (New) could not be classified as *T*=1 or *T*=3 due to large sequence insertions and no clear presence of
180 T3-motifs or E-loop insertions. Interestingly, all of the mentioned sequence insertions are present in
181 loops exposed on the outer surface of the encapsulin compartment (Supplementary Fig. 2C). The distinct
182 character of New capsids is additionally supported by the fact that all of them are found in similar gene
183 clusters that are distinct from other encapsulin loci. These clusters often contain genes encoding
184 proteins related to lipid/isoprenoid metabolism and a likely hexameric P-loop NTPase (Supplementary
185 Fig. 3).

186 All characterized encapsulins were able to assemble into nanocompartments when heterologously
187 produced in *E. coli*, highlighting the inherent robustness and assembly efficiency of encapsulins.
188 Furthermore, these assembled encapsulin nanocompartments could be isolated for biophysical and

189 biochemical analyses. We characterized 3 examples each of the *T*=1, *T*=3 and New clusters. We picked
190 sequences that are diverse both in terms of phylogenetic origin and core cargo type. After heterologous
191 expression and purification (Supplementary Fig. 2D), negative-stain transmission electron microscopy
192 (TEM) was used to visualize encapsulins. As predicted, all *T*=1 type encapsulins assemble into small
193 capsids of 22 (*Burkholderia xenovorans* and *Escherichia coli*) or 23 nm (*Streptomyces* sp. AA4) in average
194 diameter (Fig. 3B and C). The representatives chosen from the *T*=3 cluster were clearly different and as
195 hypothesized resulted in larger capsids. Interestingly, 2 of the 3 capsids were larger than expected with
196 average diameters of 37 (*Bacillaceae bacterium* MTCC 10057) and 38 nm (*Clostridium thermocellum*)
197 while *Kuenenia stuttgartiensis* capsids were 33 nm in size, similar to the previously reported *M. xanthus*
198 encapsulin capsids (32 nm). The representatives chosen from the New sequence cluster stemmed from
199 3 different phyla and assembled into larger capsids of 35 (Cyanobacteria: *Acaryochloris marina*), 36
200 (Proteobacteria: *Methylocapsa acidiphila*) and 37 nm (Actinobacteria: *Geodermatophilaceae*
201 URHB0062), similar in appearance to *T*=3 capsids. Overall, all investigated encapsulin capsids showed
202 very uniform size distributions with standard deviations between 0.9 (*Streptomyces* sp. AA4) and 2.1 nm
203 (*K. stuttgartiensis*) (Fig. 3C).

204 Certain core cargo types are confined to specific sequence clusters. We mapped the core cargo types of
205 all identified systems onto the SSN (Fig. 3A). Except for Flp-type systems, which were present in both the
206 *T*=1 and *T*=3 sequence clusters, all other core cargo types were confined to a specific capsid type. Peroxi
207 and Heme systems could only be found in the *T*=1 cluster while Geobac and NIR-HAO systems were only
208 present in the *T*=3 cluster. The match of core cargo types with a specific capsid size implies that different
209 capsid sizes have been adapted to serve particular functions.

210 ***A new hemerythrin cargo protects cells from oxidative and nitrosative stress in an encapsulation-***
211 ***dependent manner***

212 Hemerythrins are 4 helix bundle proteins that often form homo- or heterooligomeric complexes with
213 one dinuclear iron center per subunit. In prokaryotes, hemerythrin-like domains have recently been
214 proposed to be involved in O_2 and NO sensing and in the regulation of oxidative stress response[27].

215 Hemerythrins, predicted to fold into a 4 helix bundle (Supplementary Fig. 4A), are a new core cargo type
216 (Heme) in encapsulin systems. Heme core operons generally consist of the encapsulin capsid gene and a
217 hemerythrin containing a C-terminal TP encoded directly upstream (Fig. 4A). In one species (*Sporichthya*
218 *polymorpha* DSM 43042) a second hemerythrin can be found directly downstream of the encapsulin.
219 Most organisms containing a Heme system encode BfrB as an additional secondary cargo at a separate
220 locus in their genomes while in *Pseudonocardia dioxanivorans* CB1190 a Peroxi secondary cargo is
221 present.

222 Hemerythrin cargo is encapsulated by and co-purifies with encapsulin particles in a TP-dependent
223 manner. We expressed the *Streptomyces* sp. AA4 Heme core operon in *E. coli*. After capsid purification,
224 negative-stain TEM was used for particle visualization (Fig. 4B). Compared with capsids resulting from
225 the expression of the encapsulin gene alone, Heme core operon particles contain additional protein
226 density in the compartment interior. In many cases, cargo was organized in a 5- or 6-fold symmetrical
227 manner appearing as puncta associated with the interior surface of encapsulin particles (Fig. 4B insets
228 and Supplementary Fig. 4B). To confirm that the observed cargo was indeed hemerythrin, we compared
229 SDS-PAGE gels of purified encapsulin and Heme core operon capsids (Fig. 4C). As a control, particles of a
230 system where the C-terminal 12 amino acids of the hemerythrin cargo were removed was used. Only in
231 the wild-type system did hemerythrin co-purify with encapsulin particles confirming the dependence of
232 hemerythrin encapsulation on a C-terminal TP. Based on gel densitometry analysis ca. 20 molecules of
233 hemerythrin were encapsulated per 60 subunit capsid. To investigate the oligomerization state of
234 hemerythrin cargo in the absence of encapsulin we performed analytical size exclusion chromatography
235 (Fig. S4C). We found that hemerythrin cargo was present as a stable dimer in solution.

236 UV-Vis spectroscopy reveals that the diiron center of encapsulated Heme is protected from strong
237 reducing agents by the encapsulin capsid. Purified Heme core operon capsids showed 2 main absorption
238 peaks at 348 and 404 nm (as-isolated) dependent on the presence of hemerythrin, similar to previously
239 reported spectra of the met-form of hemerythrins where both iron centers are present in their ferric
240 (Fe^{3+}) but oxygen-free form (Fig. 4D)[28]. A clear change in the absorption spectrum upon dithionite
241 reduction occurs with the appearance of a new absorption peak at 427 nm. Following dithionite
242 treatment dinuclear iron proteins usually lose all absorption features in this region resulting from the
243 destruction of their metal center. Together, these results indicate that encapsulation protects the metal
244 center from being destroyed by high concentrations of strong reducing agents. Further UV-Vis analysis
245 of non-encapsulated hemerythrin cargo confirmed that without encapsulation all features in the UV-Vis
246 spectrum are lost upon dithionite incubation (Supplementary Fig. 4D).

247 The Heme containing encapsulin compartment protects *E. coli* from oxidative and nitrosative stress. We
248 carried out experiments investigating the influence of 2 stressors on the survival of *E. coli* expressing the
249 Heme core cargo system, namely hydrogen peroxide (H_2O_2) and nitric oxide (NO); hemerythrins detoxify
250 H_2O_2[29] and have been implicated in NO-sensing. Cells expressing either hemerythrin alone, encapsulin
251 alone or the complete Heme core cargo system were exposed to H_2O_2 or the NO-generator NOC-18.
252 Samples were taken after different time intervals and plated as serial dilutions for CFU-counting. A
253 strong protective effect against H_2O_2 was observed only when both components (encapsulin and
254 hemerythrin) were present while no effect could be detected for hemerythrin alone (Fig. 4E, upper
255 panel). Similarly, the Heme core cargo system was able to completely rescue *E. coli* growth when
256 exposed to NO (Fig. 4E, lower panel). In contrast to H_2O_2-exposure, expressing non-encapsulated
257 hemerythrin before applying NO stress led to ca. 50% survival compared with only ca. 20% for the
258 control (only encapsulin capsid present). Additionally, direct interaction of NO with hemerythrin was
259 confirmed via UV-Vis spectroscopy (Supplementary Fig. 4D).

260 ***A new 4 helix bundle protein found in Firmicutes shows encapsulation-dependent iron mineralization***
261 ***and oxidative stress protection***

262 Systematic analysis revealed the presence of a new core cargo type in a subset of Firmicutes annotated
263 as 'Geobacter domain of unknown function' (Geobac). In 61% of cases an additional new cargo type,
264 Ferredoxin, is closely associated with Geobac core operons (Fig. 5A). Fer is either located directly
265 downstream of the encapsulin gene, in most cases overlapping with it, or separated by one additional
266 gene whose function is unknown. No other secondary cargo types can be found in genomes encoding
267 Geobac systems. We turned to secondary and 3D structure prediction which revealed that Geobac likely
268 possesses a 4 helix bundle fold with 2 additional shorter C-terminal helices preceding the canonical TP
269 present in all core cargo types (Supplementary Fig. 4A and 5A). Surprisingly, none of the residues usually
270 associated with iron-coordinating 4 helix bundle proteins are present (Supplementary Fig. 5A).

271 Geobac cargo is encapsulated by and co-purifies with encapsulin particles in a TP-dependent fashion. To
272 further characterize the Geobac core cargo system we focused on the encapsulin, Geobac protein and
273 Fer cargo found in *Bacillaceae bacterium* MTCC 10057. *E. coli*-expression followed by particle
274 purification yielded assembled capsids (Fig. 5B). SDS-PAGE analysis showed the TP-dependent co-
275 purification of Geobac cargo with encapsulin compartments with ca. 150 molecules of Geobac per 180
276 subunit capsid (Fig. 5C). Analytical size-exclusion chromatography indicated that Geobac cargo exists in
277 an equilibrium between dimer and monomer in solution (Supplementary Fig. 5B). Taken together, the
278 above results suggest that Geobac binds to single encapsulin capsid proteins in a 1:1 or 2:1 ratio, leading
279 to a compartment where the interior surface of the majority of capsid proteins interacts with 1 or 2
280 cargo molecules.

281 Fer represents the first encapsulin cargo with an N-terminal TP and co-purifies with encapsulin particles.
282 When expressing the 3-gene operon (Geobac-Enc-Fer), no additional co-purifying cargo could be

283 observed (Fig. 5C) while the 2-gene operon (Enc-Fer) showed a band with the correct apparent
284 molecular weight expected for Fer (Supplementary Fig. 5C and D). Based on gel densitometry, 10
285 molecules of Fer co-purify per 180 subunit capsid. The identity of this protein band was confirmed to be
286 Fer via in-gel tryptic digest followed by mass spectrometry (Supplementary Fig. 5E). This suggests that
287 the N-terminal TP found in Fer is a weaker targeting signal compared with other C-terminal TPs
288 explaining why initially no co-purifying Fer cargo could be observed.

289 Geobac is an encapsulation dependent iron binding protein and is able to mineralize iron *in vivo*. UV-Vis
290 spectroscopy of purified capsids showed an absorption peak at 407 nm only when both Geobac core
291 cargo components were present, which shifted to 427 nm upon dithionite exposure indicating the
292 presence of bound iron (Fig. 5D). Since many 4 helix bundle proteins are involved in iron metabolism [22],
293 we carried out experiments where Geobac-expressing cells were exposed to elevated concentrations of
294 iron. Washed cells were either fixed for TEM or subjected to inductively coupled plasma mass
295 spectrometry (ICP-MS). When cells were expressing both Geobac cargo and encapsulin electron-dense
296 puncta were observed while no such puncta where present when only encapsulin was being expressed
297 (Fig. 5E). Electron-dense material was observed in about two thirds of cells and often organized into
298 regular paracrystalline arrangements (Supplementary Fig. 6A and B). The average particle diameter was
299 23 nm (Supplementary Fig. 6C) suggesting that particles mineralize inside encapsulin compartments
300 (outer diameter: 37 nm, shell thickness: 4-5 nm). ICP-MS analysis was used to compare the iron content
301 of cells expressing different combinations of Geobac system genes. Values adjusted for the protein
302 levels of the Geobac cargo protein (Supplementary Fig. 6D) showed that only when both complete
303 Geobac cargo (with TP) and encapsulin were present could significantly elevated iron levels be observed
304 (Fig. 5F). All other strains showed only background or slightly above background levels of retained iron.
305 Interestingly, cells expressing the 3-gene operon including Fer were able to store the largest amount of
306 iron suggesting that Fer is not necessary for iron mineralization but might improve its efficiency.

307 The Geobac encapsulin system protects *E. coli* from oxidative stress in the presence of elevated levels of
308 iron and likely represents the main iron storage system in Geobac-encoding organisms. We exposed *E.*
309 *coli* cells expressing Enc, Geobac cargo or both to H_2O_2 and monitored the CFU-count over time (Fig. 5G).
310 No increase in survival could be observed when only H_2O_2 was present. Only when cells were exposed to
311 both H_2O_2 and elevated levels of iron could a clear difference be recorded.

312 ***Encapsulins in anammox bacteria***

313 Anaerobic ammonium oxidation (anammox, converting NH_4^+ and NO_2^- to N_2) carried out by anammox
314 bacteria of the phylum Planctomycetes was proposed over 50 years ago based on thermodynamic
315 calculations[30] and is now known to be responsible for over 30% of the nitrogen lost from the oceans[31].
316 The anammox process is confined to a membrane-bound organelle referred to as the anammoxosome[32].
317 This organelle is proposed to help sequester highly toxic anammox intermediates (NO, hydrazine and
318 potentially hydroxylamine) thus protecting the rest of the cell[23]. However, it is unclear how the many
319 components inside the anammoxosome are protected from for example NO generated as an
320 intermediate.

321 We identified encapsulin systems in 4 anammox genomes (*K. stuttgartiensis*, *B. sinica*, *J. caeni* and *B.*
322 *fulgida*, Fig. 6A) encoding a large fusion protein NIR-HAO and an encapsulin N-terminally fused to a
323 cytochrome domain. Anammox encapsulins harbor an additional N-terminal diheme cytochrome
324 domain connected to the encapsulin capsid protein by a ca. 35 amino acid linker rich in proline, alanine
325 and glycine (cEnc, Supplementary Fig. 7A). Based on the presence of CxxCH-motifs we identified the
326 fusion domain as a c-type cytochrome. The 2 heme binding sites both contain additional conserved but
327 different residues (1: CxxxxDCxxCH, 2: ExxxxHxxCxYxxxxCxxCH) that likely influence their coordination
328 sphere and thus redox potential (Supplementary Fig. 7A). The predicted topology of encapsulin capsids

329 results in the N-terminus of capsid proteins protruding toward the interior of the assembled
330 compartment, leading to a particle whose inner surface is lined with diheme cytochrome domains.

331 In all 4 encapsulin loci identified in anammox bacteria a gene encoding a 2-domain fusion protein
332 (annotated as NIR: nitrite reductase (2 cupredoxin motifs) and HAO: hydroxylamine oxidoreductase (8
333 heme binding sites)) is located directly downstream of the encapsulin gene (Fig. 6A). Although no TP was
334 present in NIR-HAO, the close association of both genes, their conservation in all 4 genomes and the fact
335 that the associated encapsulin was an unusual fusion protein, led us to hypothesize that NIR-HAO might
336 represent a new type of cargo.

337 Anammox encapsulins assemble into stable capsids in the presence and absence of their N-terminal c-
338 type cytochrome fusion domain when produced in *E. coli*. We expressed the fusion encapsulin cEnc (*K.*
339 *stuttgartiensis*) as well as a mutant missing the N-terminal cytochrome domain (Enc) under anaerobic
340 conditions in *E. coli* followed by purification and TEM as well as SDS-PAGE analysis (Fig. 6B and C). Both
341 proteins are able to assemble into stable compartments, but a size difference was observed with Enc
342 forming 29 nm capsids while cEnc formed 33 nm particles. This shows that the N-terminal cytochrome
343 domain influences capsid assembly and thus size. UV-Vis spectroscopy of purified cEnc showed the
344 presence of heme that could be reduced using dithionite resulting in a shift of the 418 nm peak to
345 422 nm and the appearance of 2 new characteristic peaks at 527 and 554 nm confirming the presence of
346 c-type heme (Fig. 6D).

347 The NIR domain of the NIR-HAO cargo protein can be produced in *E. coli* under anaerobic conditions and
348 co-purifies with cEnc and Enc. First, we focused on the expression of the 2-gene operon cEnc-NIR-HAO
349 (*K. stuttgartiensis*). However, NIR-HAO was insoluble when expressed under anaerobic conditions in *E.*
350 *coli*. Difficulties in heterologously producing soluble proteins from anammox bacteria is a well-known
351 phenomenon [33]. We therefore focused on the N-terminal cupredoxin domain NIR (Supplementary Fig.

352 7C and D). We hypothesized that cargo targeting of the NIR-HAO cargo is mediated by the interaction of
353 NIR and the diheme cytochrome domain of cEnc based on studies showing direct interaction of
354 homologous proteins [34]. Anaerobically expressing NIR and the 2-gene operons consisting of cEnc/Enc
355 and NIR in *E. coli* indeed yielded soluble NIR (Fig. 6E). NIR co-purified with both cEnc and Enc with ca. 30
356 (cEnc) and ca. 15 (Enc) copies of NIR per 180mer capsid (Supplementary Fig. 7E). The decrease in the
357 amount of co-purifying NIR for the Enc system cannot be explained by the difference in size between
358 cEnc and Enc alone indicating that the presence of the diheme cytochrome domain improves cargo
359 loading. Based on these results, we propose that NIR-HAO is encapsulated by the fusion encapsulin cEnc.

360 **Discussion**

361 Here, we systematically identify and analyze nanocompartment gene clusters in bacterial and archaeal
362 genomes and classify them into core cargo groups. We establish a predictive method to organize
363 encapsulin capsid proteins into 4 distinct families, reflecting their size, cargo association and function.
364 We further experimentally characterize 3 newly discovered core cargo systems for assembly, cargo
365 targeting and physiological function establishing their involvement in oxidative and nitrosative stress
366 resistance, iron homeostasis and the anammox process.

367 The newly identified Heme core cargo system assembles into capsids of the *T*=1 class. The expression of
368 the core operon in *E. coli* confers H_2O_2 and NO resistance indicating a protective capacity of the
369 encapsulin system. Previous reports illustrated that hemerythrin model complexes and mutants are able
370 to detoxify H_2O_2 via its disproportionation into O_2 and H_2O[29, 35]. A similar mechanism in an encapsulation-
371 dependent manner, is likely responsible for the observed increase in survival upon H_2O_2 exposure when
372 the complete Heme core cargo system is present. Alternatively, increased survival could stem from
373 efficient sequestration inside the encapsulin compartment or a combination of both active
374 encapsulation-dependent detoxification and sequestration. The partial rescue from NO toxicity observed

375 for cells expressing Heme alone could indicate that resistance is mainly based on NO-binding via
376 hemerythrin and not active detoxification. Encapsulation would then lead to a more efficient
377 sequestration of NO, preventing toxic downstream reactions with O_2, iron or thiols more thoroughly
378 than free hemerythrin.

379 The newly identified encapsulin cargo protein Geobac, a 4 helix bundle protein found in Firmicutes, is
380 able to mineralize iron. In 61% of identified Geobac-containing gene clusters, a third gene encoding the
381 new Fer cargo type was identified. This arrangement is reminiscent of bacterioferritin-associated
382 ferredoxins which have been shown to improve mobilization of mineralized iron from bacterioferritins[36].
383 Fer in Geobac systems could similarly act as an electron-shuttle involved in mineralization or
384 mobilization of iron stored inside the much larger encapsulin compartments. In the presence of elevated
385 iron levels, cells expressing the Geobac core cargo system exhibited improved viability upon H_2O_2
386 exposure. This can be explained by the efficient sequestration of intracellular free iron when the
387 complete Geobac system is present leading to a decrease of toxic ROS-generating Fenton reactions[37]. In
388 addition, iron mineralization associated with ferroxidase activity is known to be able to actively remove
389 H_2O_2 in Flp-type proteins[38]. Based on the above results and the fact that all Firmicutes harboring Geobac
390 systems do not encode classical ferritins (Ftn) or bacterioferritins (BfrA or BfrB), we propose that Geobac
391 encapsulin operons represent the main strategy for iron storage in these organism. The fact that 2
392 conceptually similar but evolutionarily not closely related systems (ferritins and Geobac encapsulins)
393 exist to address the same essential function (iron homeostasis) highlights the power of convergent
394 evolution.

395 The presence of encapsulins in anammox bacteria is of particular significance given their role in the
396 global nitrogen cycle. Anammox encapsulins are fusion proteins where the encapsulin capsid protein
397 carries a unique N-terminal cytochrome domain. The capsid was shown to assemble into smaller
398 (33 nm) capsids than the other 2 *T*=3 encapsulins analyzed in this study (37 and 38 nm). The N-terminus

399 of encapsulin capsid proteins protrudes towards the interior of the assembled compartment. Thus, the
400 presence of a unique N-terminal domain likely influences capsid assembly and could explain the
401 differing capsid size observed for *K. stuttgartiensis*. All encapsulin loci identified in anammox genomes
402 also possess a conserved TP-less cargo protein NIR-HAO located directly downstream of cEnc. Anammox
403 genomes can contain up to 10 homologs annotated as HAOs (hydroxylamine oxidoreductases) with most
404 of them not having been assigned a physiological function[23]. The HAO domain present in the unique
405 fusion protein NIR-HAO is likely involved in reductive catalysis based on the absence of a heme-
406 coordinating tyrosine residue empirically found to be predictive of oxidative or reductive modes of HAO
407 function[39]. Encapsulation of 3 domains (diheme c-type cytochrome, NIR and HAO) inside a protein
408 compartment suggests that co-localization and sequestration play key parts in this protein organelles'
409 function. A protein shell would act as a barrier confining toxic intermediates sequestered or generated
410 inside the encapsulin to a dedicated cellular space. Such a system could function in sequestering toxic
411 reactions involved in the anammox process, as a detoxification system inside the anammoxosome and in
412 recycling intermediates lost through diffusion.

413 The widespread occurrence of protein-based organelles in prokaryotes demonstrates that many
414 bacteria and archaea employ sophisticated compartmentalization mechanisms to spatially organize and
415 regulate their metabolism and adapt to dynamic and hostile environments. Encapsulins are generally
416 found within a subset of a given lineage, often occupying unusual habitats, which argues that they were
417 acquired via horizontal gene transfer rather than vertical inheritance. Encapsulin function is based on
418 the targeted encapsulation of functional protein components and enzymatic functions often involved in
419 carrying out toxic reactions. Thus, we propose that encapsulin systems are a general strategy found in
420 microbes to sequester toxic transformations and molecules and serve as specific storage compartments.

421 **Methods**

422 **Computational analysis of microbial genomes and encapsulin gene clusters**

423 Genome-mining for encapsulin capsids was initiated by carrying out PSI-BLAST[40] searches using the
424 following experimentally confirmed capsid proteins as queries: WP_010865203.1 (*T. maritima*),
425 WP_009884820.1 (*B. linens*), WP_020909834.1 (*R. erythropolis*), ABF87797.1 (*M. xanthus*),
426 WP_048059055.1 (*P. furiosus*) and NP_215313.1 (*M. tuberculosis*). Five iterations where run using the
427 following parameters: Expect threshold: 1, word size: 3, matrix: BLOSUM62, gap costs: Existence: 11
428 Extension: 1, compositional adjustments: conditional compositional score matrix adjustment, PSI-
429 threshold: 0.0005. All hits were combined and the surroundings (10 kb) of the encapsulin gene inspected
430 for the presence of genes annotated as phage-related using BLASTp with default settings. If the case,
431 these hits were deleted. This resulted in a list of 909 encapsulin-encoding loci.
432 Phylogenetic analysis was based on a Clustal Omega (ClustalO)[41] alignment carried out using the default
433 settings of the Multiple Sequence Alignment online tool of the European Molecular Biology Laboratory's
434 European Bioinformatics Institute (EMBL-EBI). A nearest-neighbor phylogenetic tree based on the
435 ClustalO alignment was generated using Geneious 9.1.4 with the HK97 bacteriophage capsid protein as
436 the outgroup (NP_037666.1) and then annotated and visualized using the Interactive Tree of Life (iTOL
437 v3) online server[42].
438 To identify core cargo proteins present in the set of encapsulin-encoding genomes MultiGeneBlast
439 (MGB)[20]searches using the respective encapsulin proteins and a TP consensus sequence based on
440 characterized core cargo proteins (NP_228595.1 WP_044480584.1 NP_215314.1 WP_009884819.1
441 ABF88760.1, SDGSLGIGSLKRS) as dual queries were carried out. The consensus was generated using
442 Geneious 9.1.4 and was based on ClustalO alignments. MGB was run in the 'Architecture search' mode
443 with minimal sequence coverage at 20%, minimal identitiy at 20%, the maximum distance between
444 genes in locus at 4 kb and the weight of synteny conservation at 1. A custom database of all encapsulin-
445 encoding genomes generated with MGB was used. Only hits where the central residue of the hit string
446 was located closer than 15 residues from the N- or C-terminus were considered valid.

447 Secondary cargo proteins were discovered using BLASTp searches of encapsulin-encoding genomes with
448 three different TP-consensus sequences as queries. BLASTp parameters were automatically adjusted for
449 short input sequences. The first consensus was generated from all identified core cargo proteins
450 (DGSLGTIGSLKGE). The remaining consensus queries were based on BLASTp hit lists of FolB
451 (RGSVVPAGGAAV) and BfrB (DGAPPAAGGAL) previously identified in *M. tuberculosis*[19]. Alignments were
452 generated using ClustalO and the consensus obtained via Geneious 9.1.4.
453 Sequence similarity network (SSN) analysis was carried out using the Enzyme Similarity Tool of the
454 Enzyme Function Initiative[25] with input fasta files containing all protein sequences to be analyzed. After
455 the initial datasets were created we used an alignment score (based on the alignment score vs percent
456 identity plot) that would correspond to a percent identity of 20 for initial outputting and interpretation
457 of the SSN. The resulting xgmml file was imported into Cytoscape 3.3.0. Each node in the network
458 corresponds to a single protein sequence while each edge represents a pairwise connection between
459 two proteins based on a specified % identity cutoff. The cutoffs used for final outputting were 24
460 (encapsulin capsid proteins) and 39 (Flp-type proteins). The networks were visualized using the yFiles
461 organic layout option of Cytoscape 3.3.0.
462 **Molecular biology and cloning**
463 All constructs used in this study were ordered as gBlock Gene Fragments from Integrated DNA
464 Technologies (IDT). Codon usage was optimized for *E. coli* with the IDT Codon Optimization Tool with the
465 amino acid sequences of the respective proteins of interest as input. For operons that contained
466 overlapping and/or multiple genes, intergenic regions and overlapping sequences were not changed.
467 Heme, Geobac and NIR cargo constructs for characterization in the absence of encapsulin were ordered
468 containing C-terminal His_6 tags. For TP-less Heme and Geobac cargo proteins, the 12 (Heme) and 10
469 (Geobac) C-terminal residues were omitted, thus removing the TP. The native *K. stuttgartiensis* proteins
470 cEnc and NIR-HAO contain N-terminal signal peptides reminiscent of twin-arginine peptides. They were

471 predicted using the SignalIP 4.1 Server[43]. For cEnc, the N-terminal 36 amino acids
472 (MVMGILNTFKKVYAVTGFFALLAVFSLSQVGSSAFA) and for NIR-HAO the N-terminal 27 amino acids
473 (MLNKSAALVPVVLAFLFLFLCFQCLYA) were omitted when ordering the respective constructs for cloning.
474 The dissected NIR domain of the didomain protein NIR-HAO (CAJ73224.1) was based on the 300 N-
475 terminal residues of the signal peptide-less protein based on domain annotations using Pfam, NCBI-CDD
476 and PROSITE. The N-terminal diheme cytochrome domain of cEnc was removed by omitting the 50
477 amino acids at the start of the signal peptide-less cEnc protein resulting in Enc. Gibson Assembly®
478 Master Mix was obtained from New England BioLabs (NEB). DNA sequencing was carried out by
479 GENEWIZ. NEB Turbo Competent *E. coli* cells were used for all cloning procedures while BL21 (DE3) Star
480 Competent *E. coli* (NEB) cells were used for protein production and all other experiments. The vectors
481 pETDuet1 and pCDFDuet1 were used for all cloning procedures. For the construction of expression
482 constructs, Gibson Assembly was employed. The respective gBlock Gene Fragments containing 20 bp
483 overlaps for direct assembly were combined with NdeI and PacI digested pETDuet1 or pCDFDuet1
484 yielding the constructs/strains listed in Table S1. Chemically competent *E. coli* Turbo cells were
485 transformed and the resulting plasmids confirmed by sequencing.

486 **Expression and purification of proteins and protein compartments**

487 All expression experiments were carried out in lysogeny broth (LB) supplemented with ampicillin (100
488 μg/mL), spectinomycin (100 μg/mL) or both. Size exclusion chromatography/gelfiltration for capsid
489 purification was performed with an ÄKTA Explorer 10 (GE Healthcare Life Sciences) equipped with a
490 HiPrep 16/60 Sephacryl S-500 HR column (GE Healthcare Life Sciences). For analytical size exclusion to
491 determine oligomerization state in solution a Superdex 200 10/300 GL column (GE Healthcare Life
492 Sciences) was employed. Protein samples were desalted and concentrated with Amicon Ultra Filters
493 from Millipore. For SDS-PAGE analysis, Novex Tris-Glycine Gels (ThermoFisher Scientific) were used. DNA

494 and protein concentrations were measured using a Nanodrop ND-1000 instrument (PEQLab) and UV-Vis
495 spectra were recorded with the same instrument.
496 Assembled and sequence-confirmed plasmids were used to transform *E. coli* BL21 (DE3) Star cells (ca.
497 0.5 ng total DNA). For co-transformations of two constructs ca. 15 ng of each plasmid was used.
498 For standard aerobic protein expressions 50 mL LB was inoculated (1:50) using an over-night culture,
499 grown at 37°C and 200 rpm to an OD_{600} of 0.5 and then induced with IPTG (final concentration: 0.1 mM).
500 Cultures were grown at 30°C for 18 h, harvested via centrifugation (4000 rpm, 15 min, 4°C) and the
501 pellets either immediately used or flash frozen in N_2(l) and stored at -20°C.
502 For anaerobic expressions of the *K. stuttgartiensis* constructs cEnc, Enc and NIR, LB medium was
503 inoculated (1:50) and initially grown aerobically to an OD_{600} of 0.5. The culture was then made anoxic
504 through vigorous purging using argon. For all cEnc containing expressions, hemin (stock: 500 μM in 10
505 mM KOH, final concentration: 10 μM) and freshly made $FeSO_4$ (stock: 200 mM in water, final
506 concentration: 10 μM) were added. For NIR expressions $CuCl_2$ (stock: 200 mM in water, final
507 concentration: 2 μM) was added. After adding IPTG to a final concentration of 0.1 mM, the cultures
508 were transferred to Vacu-Quik jars (Almore Internationl, inc.). Two BD GasPak EZ satchets were added.
509 This was followed by two rounds of air removal and argon flushing of the jar. Then cultures were
510 incubated at 30°C for 18 h under an argon atmosphere. Cells were centrifuged (4000 rpm, 15 min, 4°C)
511 and the pellets either immediately used or frozen in N_2(l) and stored at -20°C.
512 For encapsulin and His-tagged protein purifications, pellets were thawed, resuspended in 5 mL PBS (pH
513 7.4) buffer, then lysozyme (final concentration: 1 mg/mL) and DNaseI (final concentration: 1 μg/mL)
514 were added and the cells incubated for 20 min on ice. Cell suspensions were subjected to sonication
515 using a 550 Sonic Dismembrator (FisherScientific). Power level 3.5 was used with a pulse time of 8 sec
516 and an interval of 10 sec. Total pulse time was 3 min. Cell debris was subsequently removed through

517 centrifugation (8000 rpm, 15 min, 4°C). The cleared supernatant was then used either for protein affinity
518 or encapsulin particle purification.
519 His-tagged proteins were purified using Ni-NTA agarose resin (Qiagen) via batch Ni-NTA affinity
520 procedure following the supplier's instructions. Buffer A (50 mM Tris, pH 8, 300 mM NaCl, 2 mM β-
521 mercaptoethanol, 5% glycerol, 20 mM imidazol) was used to wash resin after protein binding and buffer
522 B (50 mM Tris, pH 8, 300 mM NaCl, 2 mM β-mercaptoethanol, 5% glycerol, 250 mM imidazol) was used
523 to elute bound protein. Samples were concentrated and dialyzed using Amicon filters and PBS (pH 7.4)
524 buffer and evaluated using SDS-PAGE. Further analyses were carried out directly or the next day with
525 protein being stored on ice.
526 To cleared lysates (5 mL) containing encapsulin particles 0.1 g NaCl and 0.5 g of PEG-8000 was added
527 (ca. 10% w/v final concentration), followed by incubation on ice for 30 min. The precipitate was
528 collected through centrifugation (8000 rpm, 15 min, 4°C), suspended in 3 mL PBS buffer and filtered
529 using a 0.2 μm syringe filter. The samples were then subjected to size exclusion chromatography using
530 PBS buffer and a flow rate of 1 mL/min. Fractions were evaluated using SDS-PAGE analysis and protein
531 compartment containing fractions were combined and concentrated using Amicon filters. The samples
532 were either directly subjected to additional analysis or stored on ice overnight. The relative ratios
533 adjusted for molecular mass of encapsulin capsid proteins and co-purifying cargo was determined using
534 the Gel Analyzer of the open source image processing package Fiji based on ImageJ 1.51f.
535 **Transmission electron microscopy (TEM)**
536 200 Mesh Gold Grids (FCF-200-Au, EMS) were used for all TEM experiments. TEM experiments of fixed
537 cells or negatively stained protein samples were carried out at the HMS Electron Microscopy Facility
538 using a Tecnai G2 Spirit BioTWIN instrument.
539 For negative-staining TEM, encapsulin samples were diluted to 1-10 μM using Hepes buffer (10 mM
540 Hepes, pH 7.4) and subsequently adsorbed onto formvar/carbon coated gold grids. Grids were glow-

541 discharged using a 100x glow discharge unit (EMS) to increase their hydrophilicity (10 sec, 25 mA) before
542 applying 5 μL of diluted sample. After 1 min adsorption time, excess liquid was blotted off using
543 Whatman #1 filterpaper, washed with H_2O and floated on a 10 μL drop of staining solution (0.75%
544 uranyl formate in H_2O) for 35 sec. After removal of excess liquid samples were ready for TEM analysis at
545 80 keV.
546 For TEM analysis of fixed cells, 0.5 mL of bacterial culture was fixed by adding fixative (1:1 v/v, 1.25%
547 formaldehyde, 2.5% glutaraldehyde, 0.03% picric acid in 0.1 M sodium cacodylate buffer, pH 7.4). The
548 sample was then incubated at 25°C for 1 h and centrifuged for 3 min at 3000 rpm. The sample
549 containing pellet and supernatant in the same tube was further incubated for 6-18 h at 4°C. Cells were
550 subsequently washed three times in cacodylate buffer, 4 times with maleate buffer pH 5.15 followed by
551 staining with 1% uranyl acetate for 30 min. Then, the sample was dehydrated (15 min 70% ethanol, 15
552 min 90% ethanol, 2 x 15 min 100% ethanol) and exposed to propyleneoxide for 1 h. For infiltration, a
553 mixture of Epon resin and proylenoxide (1:1) was incubated for 2 h at 25°C before moving it to an
554 embedding mold filled with freshly mixed Epon. The sample was allowed to sink and subsequently
555 moved to a polymerization oven (24 h, 60°C). Ultrathin sections (60-90 nm) were then cut at -120°C
556 using a cryo-diamond knife (Reichert cryo-ultramicrotome) and transferred to formvar/carbon coated
557 grids.
558 **Determination of average particle diameter**
559 To determine the average diameters of encapsulin particles and electron-dense puncta resulting from
560 Geobac-expression in the presence of elevated levels of iron, TEM micrographs were analyzed using the
561 open source image processing package Fiji based on ImageJ 1.51f. Micrographs were converted to 8-bit
562 binary images, thresholded and processed using the particle analyzer plugin. For encapsulin capsids at
563 least 500 particles were analyzed, while 141 electron-dense puncta (Geobac) were recorded. The
564 diameters reported are based on Fiji Feret diameter output values.

565 **UV-Vis analysis of Heme, Geobac and cEnc**

566 After purification, as-isolated (oxidized) samples of Heme, Geobac, cEnc and loaded and empty
567 encapsulin capsids were directly subjected to UV-Vis analysis (Nanodrop ND-1000). To study the
568 interaction of Heme, Geobac and cEnc with different small molecule partners, samples were made
569 anoxic through repeated removal of air and flushing with argon using glass vials sealed with rubber
570 septa. Samples in PBS (100 μM) were incubated with sodium dithionite (excess: ca. 50 mM), sodium
571 azide (500 μM), sodium cyanide (500 μM), H_2O_2 (500 μM) or diethylenetriamine/nitric oxide (NOC-18,
572 6 mM) for 5 min on ice before carrying out measurements.

573 **Oxidative and nitrosative stress survival assays**

574 Overnight cultures of strains expressing different components of the Heme and Geobac encapsulin
575 systems were grown at 37°C and 200 rpm. They were used to inoculate 50 mL LB cultures (1:25) which
576 were grown at 37°C to an OD_{600} of 0.5, then induced using IPTG (0.1 mM) and incubated at 30°C and
577 200 rpm for 2 h. Cultures were then diluted to an OD_{600} of 0.3 using fresh LB. H_2O_2 (final concentration:
578 0.5 mM) or NOC-18 (final concentration: 6 mM) were then added and cultures incubated at 37°C and
579 200 rpm in the dark. For Geobac, cultures with and without additional $FeSO_4$ (250 μM) were prepared.
580 Controls did not contain H_2O_2/NOC-18. Samples were taken after 0, 1, 2 and 4 h and diluted (1:10-
581 1:1000) using fresh LB. 100 μL of each dilution was then spread on antibiotic-containing LB agar plates
582 which were incubated at 37°C for 18 h. Colonies on plates were manually counted the next day. All
583 experiments were carried out at least in triplicate. Counts were normalized using non-
584 H_2O_2/NOC-18 treated cultures and expressed as survival percentages.

585 **Inductively coupled plasma mass spectrometry (ICP-MS)**

586 ICP-MS measurements were carried out at the Trace Metals Lab at Harvard T.H. Chan School of Public
587 Health. For the analysis of iron content of cells expressing different Geobac components, 1 mL (OD_{600} =
588 2.4) of induced over-night culture was pelleted and then washed four times with H_2O. Pellets were then

589 prepared for ICP-MS analysis using nitric acid resulting in a final concentration of 2% (w/v) and
590 measured with a Perkin Elmer Elan DRC-II Inductively Coupled Plasma-Mass Spectrometer. Reported
591 results are based on three independent measurements per sample.

592 **In vivo iron mineralization assays**

593 Overnight cultures of cells expressing Geobac constructs were used to inoculate 50 mL LB medium and
594 grown to an OD_{600} of 0.5. Before induction with 0.1 mM IPTG, 250 μM freshly prepared $FeSO_4$ (in water)
595 was added. The cultures were then incubated at 30°C for 18 h. Then cells were fixed for TEM analysis.

596 **Protein identification**

597 Protein identification of SDS-PAGE gel bands was carried out at the Harvard Medical School Taplin Mass
598 Spectrometry Facility. Coomassie Blue stained gels were destained to clear background. Single bands
599 were excised with as little excess empty gel as possible. Excised gel bands were cut into approximately 1
600 mm^3 pieces. Gel pieces were washed and dehydrated with acetonitrile for 10 min. Pieces were then
601 completely dried in a speed-vac. Rehydration of the gel pieces was done with 50 mM NH_4HCO_3 solution
602 containing 12.5 ng/μl modified sequencing-grade trypsin (Promega, Madison, WI) at 4°C. After 45 min,
603 excess trypsin solution was removed and replaced with 50 mM NH_4HCO_3 solution to just cover the gel
604 pieces. Samples were incubated at 37°C room overnight. Peptides were extracted by removing the
605 NH_4HCO_3 solution, followed by one wash with 50% acetonitrile and 1% formic acid. The extracts were
606 then dried in a speed-vac (1 h). The samples were stored at 4°C until analysis. On the day of analysis the
607 samples were reconstituted in 5-10 μL of HPLC solvent A (2.5% acetonitrile, 0.1% formic acid). A nano-
608 scale reverse-phase HPLC capillary column was created by packing 2.6 μm C18 spherical silica beads into
609 a fused silica capillary (100 μm inner diameter, 30 cm length) with a flame-drawn tip. After equilibrating
610 the column each sample was loaded via a Famos auto sampler (LC Packings, San Francisco, CA) onto the
611 column. A gradient was formed and peptides were eluted with increasing concentrations of solvent B
612 (97.5% acetonitrile, 0.1% formic acid). As peptides eluted they were subjected to electrospray ionization

613 and then entered into an LTQ Orbitrap Velos Pro ion-trap mass spectrometer (Thermo Fisher Scientific,
614 Waltham, MA). Peptides were detected, isolated, and fragmented to produce a tandem mass spectrum
615 of specific fragment ions for each peptide. Peptide sequences (and hence protein identity) were
616 determined by matching protein databases with the acquired fragmentation pattern using Sequest
617 (Thermo Fisher Scientific, Waltham, MA). All databases include a reversed version of all the sequences
618 and the data was filtered to between a one and two percent peptide false discovery rate.

619 **References**

620 1. Diekmann, Y. & Pereira-Leal, J.B. Evolution of intracellular compartmentalization. *Biochem. J.*
621 **449**, 319-331 (2013).
622 2. Martin, W. Evolutionary origins of metabolic compartmentalization in eukaryotes. *Philosophical*
623 *transactions of the Royal Society of London. Series B, Biological sciences* **365**, 847-855 (2010).
624 3. Schrader, M., Godinho, L.F., Costello, J.L. & Islinger, M. The different facets of organelle
625 interplay-an overview of organelle interactions. *Frontiers in cell and developmental biology* **3**, 56
626 (2015).
627 4. Cornejo, E., Abreu, N. & Komeili, A. Compartmentalization and organelle formation in bacteria.
628 *Curr. Opin. Cell Biol.* **26**, 132-138 (2014).
629 5. Giessen, T.W. & Silver, P.A. Encapsulation as a Strategy for the Design of Biological
630 Compartmentalization. *J. Mol. Biol.* (2015).
631 6. Kerfeld, C.A. & Erbilgin, O. Bacterial microcompartments and the modular construction of
632 microbial metabolism. *Trends Microbiol.* **23**, 22-34 (2015).
633 7. Kerfeld, C.A. & Melnicki, M.R. Assembly, function and evolution of cyanobacterial
634 carboxysomes. *Curr. Opin. Plant Biol.* **31**, 66-75 (2016).
635 8. Hintze, K.J. & Theil, E.C. Cellular regulation and molecular interactions of the ferritins. *Cell. Mol.*
636 *Life Sci.* **63**, 591-600 (2006).
637 9. Pfeifer, F. Distribution, formation and regulation of gas vesicles. *Nat. Rev. Microbiol.* **10**, 705-715
638 (2012).
639 10. Chen, A.H., Robinson-Mosher, A., Savage, D.F., Silver, P.A. & Polka, J.K. The bacterial carbon-
640 fixing organelle is formed by shell envelopment of preassembled cargo. *PloS one* **8**, e76127
641 (2013).
642 11. Giessen, T.W. Encapsulins: microbial nanocompartments with applications in biomedicine,
643 nanobiotechnology and materials science. *Curr. Opin. Chem. Biol.* **34**, 1-10 (2016).
644 12. Sutter, M. *et al.* Structural basis of enzyme encapsulation into a bacterial nanocompartment.
645 *Nat. Struct. Mol. Biol.* **15**, 939-947 (2008).
646 13. Rurup, W.F., Snijder, J., Koay, M.S., Heck, A.J. & Cornelissen, J.J. Self-sorting of foreign proteins
647 in a bacterial nanocompartment. *J. Am. Chem. Soc.* **136**, 3828-3832 (2014).
648 14. McHugh, C.A. *et al.* A virus capsid-like nanocompartment that stores iron and protects bacteria
649 from oxidative stress. *EMBO J.* **33**, 1896-1911 (2014).
650 15. He, D. *et al.* Structural characterization of encapsulated ferritin provides insight into iron storage
651 in bacterial nanocompartments. *eLife* **5** (2016).

652 16. Akita, F. *et al.* The crystal structure of a virus-like particle from the hyperthermophilic archaeon
653 Pyrococcus furiosus provides insight into the evolution of viruses. *J. Mol. Biol.* **368**, 1469-1483
654 (2007).
655 17. Rahmanpour, R. & Bugg, T.D. Assembly in vitro of Rhodococcus jostii RHA1 encapsulin and
656 peroxidase DypB to form a nanocompartment. *FEBS J.* **280**, 2097-2104 (2013).
657 18. Valdes-Stauber, N. & Scherer, S. Isolation and characterization of Linocin M18, a bacteriocin
658 produced by Brevibacterium linens. *Appl. Environ. Microbiol.* **60**, 3809-3814 (1994).
659 19. Contreras, H. *et al.* Characterization of a Mycobacterium tuberculosis nanocompartment and its
660 potential cargo proteins. *J. Biol. Chem.* **289**, 18279-18289 (2014).
661 20. Medema, M.H., Takano, E. & Breitling, R. Detecting sequence homology at the gene cluster level
662 with MultiGeneBlast. *Mol. Biol. Evol.* **30**, 1218-1223 (2013).
663 21. Alvarez-Carreno, C., Becerra, A. & Lazcano, A. Molecular Evolution of the Oxygen-Binding
664 Hemerythrin Domain. *PloS one* **11**, e0157904 (2016).
665 22. Andrews, S.C. The Ferritin-like superfamily: Evolution of the biological iron storeman from a
666 rubrerythrin-like ancestor. *Biochim. Biophys. Acta* **1800**, 691-705 (2010).
667 23. Kartal, B. *et al.* How to make a living from anaerobic ammonium oxidation. *FEMS Microbiol. Rev.*
668 **37**, 428-461 (2013).
669 24. Radford, D. in Department of Molecular Genetics, Vol. Doctorate of Philosophy (University of
670 Toronto, Toronto, Canada; 2015).
671 25. Gerlt, J.A. *et al.* Enzyme Function Initiative-Enzyme Similarity Tool (EFI-EST): A web tool for
672 generating protein sequence similarity networks. *Biochim. Biophys. Acta* **1854**, 1019-1037
673 (2015).
674 26. Straub, K.L., Hanzlik, M. & Buchholz-Cleven, B.E. The use of biologically produced ferrihydrite for
675 the isolation of novel iron-reducing bacteria. *Syst. Appl. Microbiol.* **21**, 442-449 (1998).
676 27. Li, X. *et al.* A bacterial hemerythrin-like protein MsmHr inhibits the SigF-dependent hydrogen
677 peroxide response in mycobacteria. *Frontiers in microbiology* **5**, 800 (2014).
678 28. Hathazi, D. *et al.* Oxidative protection of hemoglobin and hemerythrin by cross-linking with a
679 nonheme iron peroxidase: potentially improved oxygen carriers for use in blood substitutes.
680 *Biomacromolecules* **15**, 1920-1927 (2014).
681 29. Okamoto, Y. *et al.* H2O2-dependent substrate oxidation by an engineered diiron site in a
682 bacterial hemerythrin. *Chemical communications* **50**, 3421-3423 (2014).
683 30. Richards, F.A. *Anoxic basins and fjordsin*. (London, UK; 1965).
684 31. Ward, B.B. & Jensen, M.M. The microbial nitrogen cycle. *Frontiers in microbiology* **5**, 553 (2014).
685 32. Fuerst, J.A. & Sagulenko, E. Nested bacterial boxes: nuclear and other intracellular
686 compartments in planctomycetes. *J. Mol. Microbiol. Biotechnol.* **23**, 95-103 (2013).
687 33. Javidpour, P. *et al.* Investigation of Proposed Ladderane Biosynthetic Genes from Anammox
688 Bacteria by Heterologous Expression in E. coli. *PloS one* **11**, e0151087 (2016).
689 34. Tsuda, A. *et al.* Structural and mechanistic insights into the electron flow through protein for
690 cytochrome c-tethering copper nitrite reductase. *Journal of biochemistry* **154**, 51-60 (2013).
691 35. Mauerer, B., Crane, J., Schuler, J., Wieghardt, K. & Nuber, B. A Hemerythrin Model Complex with
692 Catalase Activity. *Angewandte Chemie* **32**, 289-291 (2003).
693 36. Wang, Y. *et al.* Characterization of the Bacterioferritin/Bacterioferritin Associated Ferredoxin
694 Protein-Protein Interaction in Solution and Determination of Binding Energy Hot Spots.
695 *Biochemistry* **54**, 6162-6175 (2015).
696 37. Cozzi, A. *et al.* Overexpression of wild type and mutated human ferritin H-chain in HeLa cells: in
697 vivo role of ferritin ferroxidase activity. *J. Biol. Chem.* **275**, 25122-25129 (2000).

698 38. Zhao, G. *et al.* Iron and hydrogen peroxide detoxification properties of DNA-binding protein
699 from starved cells. A ferritin-like DNA-binding protein of Escherichia coli. *J. Biol. Chem.* **277**,
700 27689-27696 (2002).
701 39. Klotz, M.G. *et al.* Evolution of an octahaem cytochrome c protein family that is key to aerobic
702 and anaerobic ammonia oxidation by bacteria. *Environ. Microbiol.* **10**, 3150-3163 (2008).
703 40. Altschul, S.F. *et al.* Gapped BLAST and PSI-BLAST: a new generation of protein database search
704 programs. *Nucleic Acids Res.* **25**, 3389-3402 (1997).
705 41. Sievers, F. *et al.* Fast, scalable generation of high-quality protein multiple sequence alignments
706 using Clustal Omega. *Mol. Syst. Biol.* **7**, 539 (2011).
707 42. Letunic, I. & Bork, P. Interactive tree of life (iTOL) v3: an online tool for the display and
708 annotation of phylogenetic and other trees. *Nucleic Acids Res.* **44**, W242-245 (2016).
709 43. Petersen, T.N., Brunak, S., von Heijne, G. & Nielsen, H. SignalP 4.0: discriminating signal peptides
710 from transmembrane regions. *Nat. Methods* **8**, 785-786 (2011).

711

712 **Acknowledgments**

713 This work was supported by a Leopoldina Research Fellowship (LPDS 2014-05) from the German
714 National Academy of Sciences Leopoldina (T.W.G), the DARPA Living Foundries: 1000 Molecules grant
715 (award number: HR0011-14-C-0072; P.A.S) and the Wyss Institute for Biologically Inspired Engineering at
716 Harvard University (T.W.G and P.A.S). We thank Alina Chan and Julian Hegemann for thoughtful
717 comments on the manuscript.

718 **Author contributions**

719 T.W.G. and P.A.S designed the research and wrote the paper. T.W.G. performed experiments.

720 **Competing interests**

721 The authors declare no competing financial interests.

722

723

724

725

726

727

728 **Figures and figure legends**

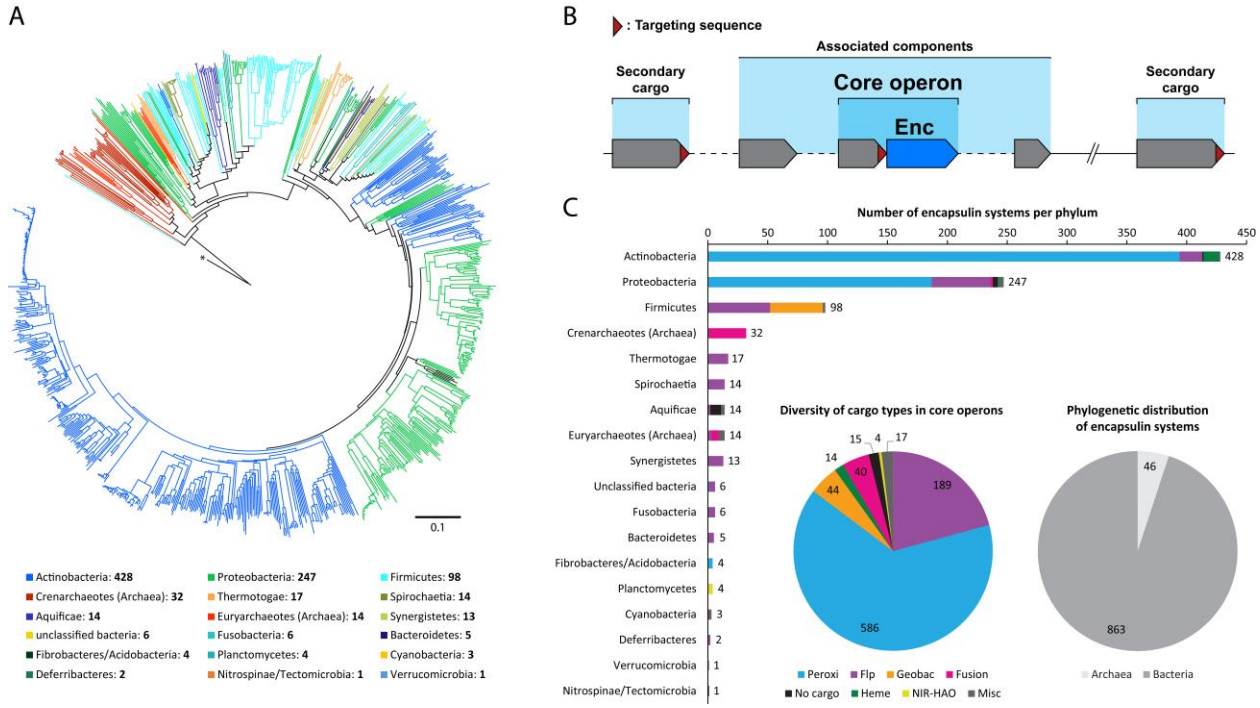

729

730 **Figure 1: Distribution, organization and diversity of encapsulin systems in prokaryotes.** (A) Nearest-
731 neighbor phylogenetic tree of 909 encapsulin capsid proteins using the major capsid protein of
732 bacteriophage HK97 as the outgroup (*) based on a ClustalOmega multiple alignment (distance scale:
733 0.1). The number of identified encapsulin systems per phylum is given below the phylogenetic tree. (B)
734 Scheme depicting the general organization of encapsulin systems. The core operon consists of an
735 encapsulin capsid gene (Enc) and a core cargo usually directly upstream. Other non-targeted but
736 functionally associated components are found in proximity to of the core operon. Additional secondary
737 cargo can be present throughout the genome. (C) Bar graph depicting the distribution of identified core
738 cargo families in bacterial and archaeal phyla. The number of systems belonging to each identified core
739 cargo type as well as the distribution of encapsulin systems in bacteria and archaea are shown as pie
740 graphs.

741

742

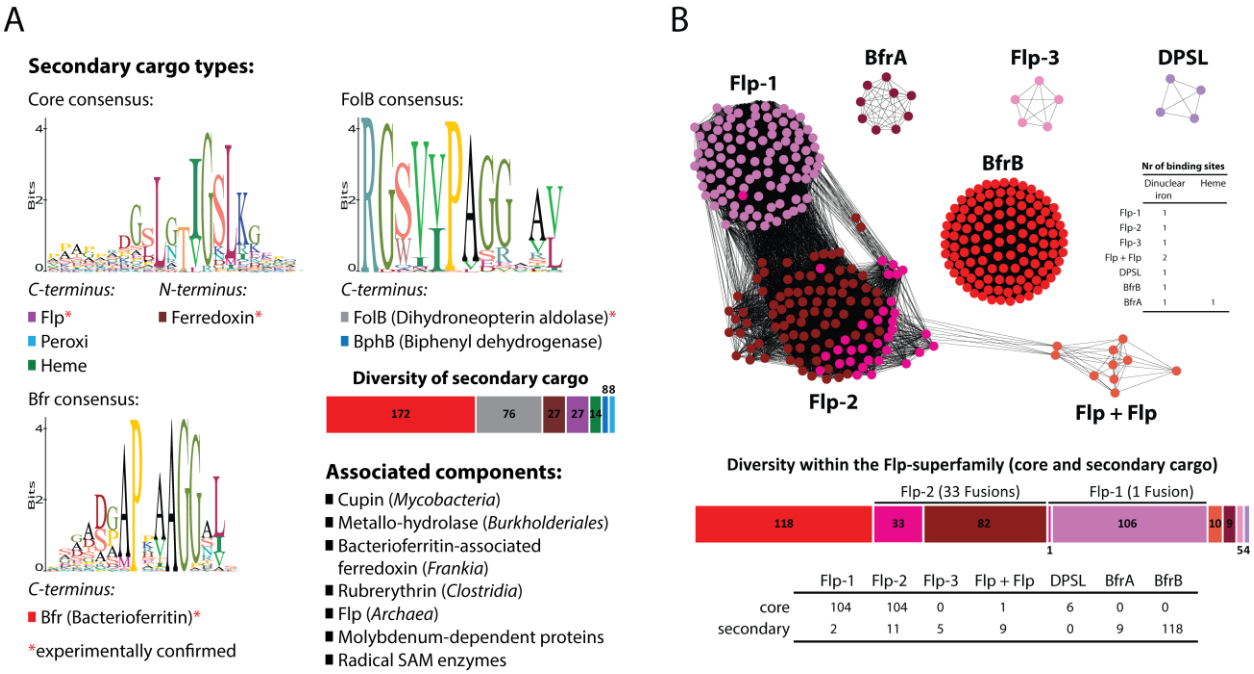

Figure 2: Secondary cargo, associated components and diversity of Flp-like cargo in encapsulin systems. (A) Shown are sequence logos of the 3 targeting peptide consensus sequences used to identify secondary cargo in all encapsulin containing genomes. The y-axis denotes positional information in bits. The secondary cargo types identified using a given consensus as a query are listed below the respective sequence logos. Experimentally confirmed secondary cargo types (either in this study or previously) are indicated with a red asterisk. The number of identified instances of different secondary cargo types are shown as a color-coded bar graph. A list of associated components identified in certain genera (shown in parentheses) is shown. (B) Sequence similarity network of all Flp-family cargo proteins identified in encapsulin systems (edge % identity: 39). The inset table indicates the presence and number of dinuclear iron centers and heme binding sites in each family. A bar graph depicts the number of proteins identified of each Flp-type with Flp-fusions depicted in pink. The bottom table shows the number of sequences of each Flp-family identified as core or secondary cargo.

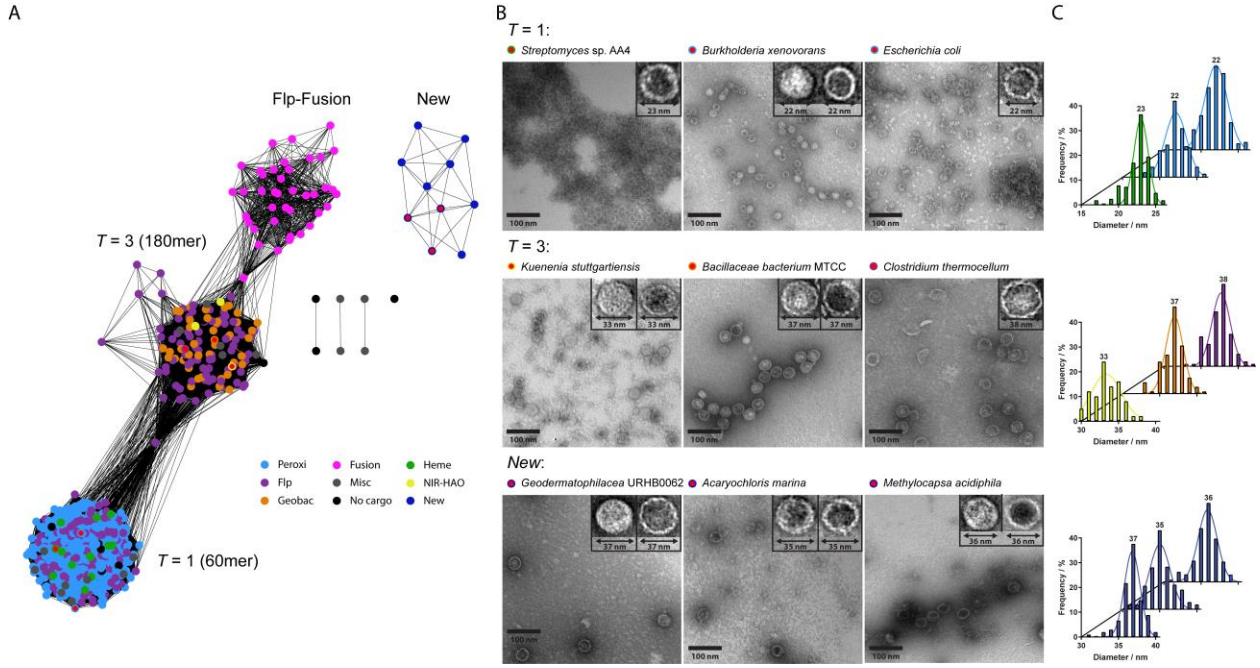

757

758 **Figure 3: Classification and characterization of encapsulin capsids.** (A) Sequence similarity network of
759 all identified encapsulin capsid proteins (edge % identity: 24). Individual nodes are colored
760 corresponding to their associated core cargo type. Red dots indicate the capsids chosen for
761 experimental characterization. (B) Negative-stain TEM micrographs of 9 encapsulin capsids from the
762 *T*=1, *T*=3 and New sequence clusters. Insets show magnified examples of each capsid. (C) Size-
763 distribution of the characterized encapsulin capsids fitted using a Gaussian fit.

764

765

766

767

768

769

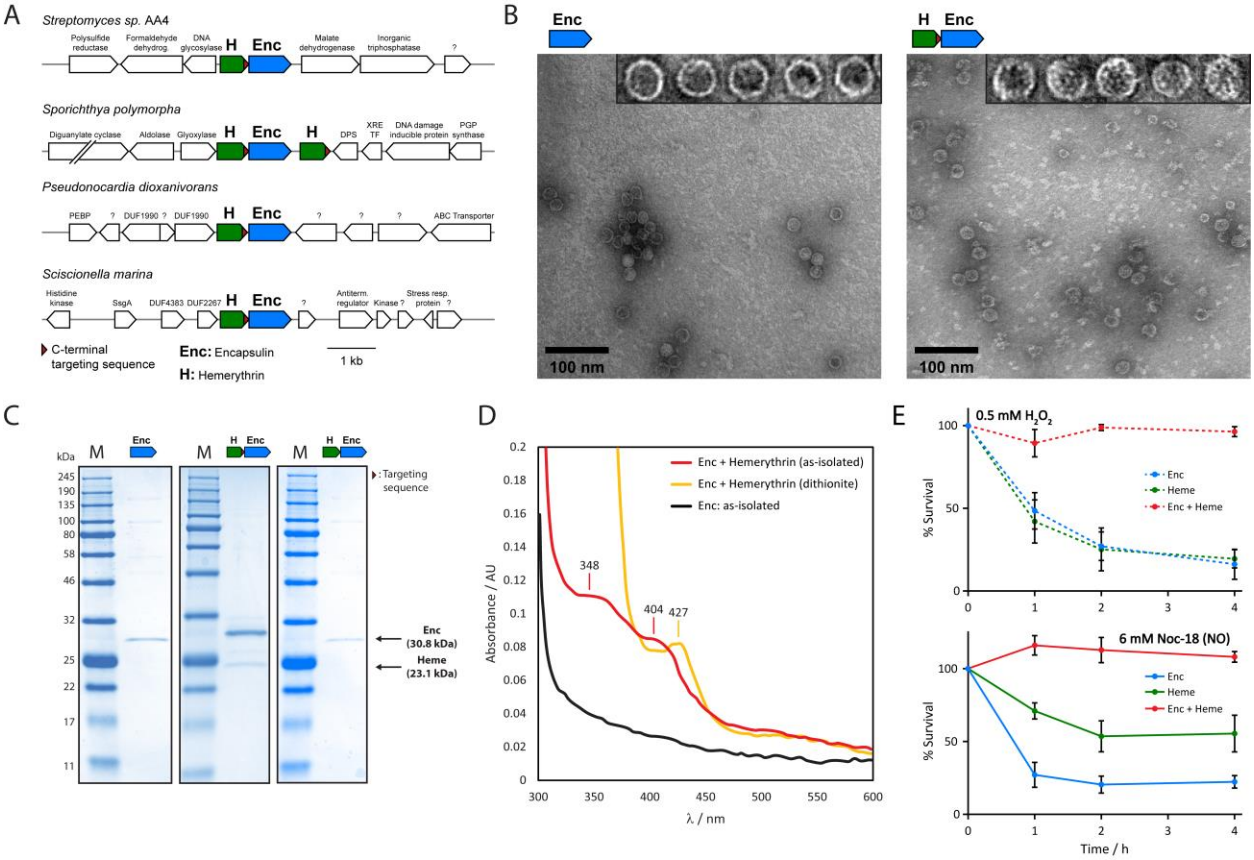

Figure 4: Characterization of the *Streptomyces* sp. AA4 Heme encapsulin system involved in oxidative and nitrosative stress resistance. (A) Selected Heme encapsulin gene clusters and their genetic surroundings. (B) Negative-stain TEM micrographs of purified encapsulin particles without (left) and with (right) Heme cargo. Insets show magnified particles. Additional protein puncta are visible when both Enc and Heme are present. (C) SDS-PAGE analysis of purified particles without (left) and with (middle) Heme. A mutant Heme missing the C-terminal TP does not co-purify with Enc particles (right). (D) UV-Vis spectroscopy of purified particles. (E) Survival of *E. coli* expressing Enc, Heme or Enc+Heme in the presence of H_2O_2 (top panel) or the NO-generator Noc-18 (lower panel). Data are represented as mean ± SD of 3 biological replicates.

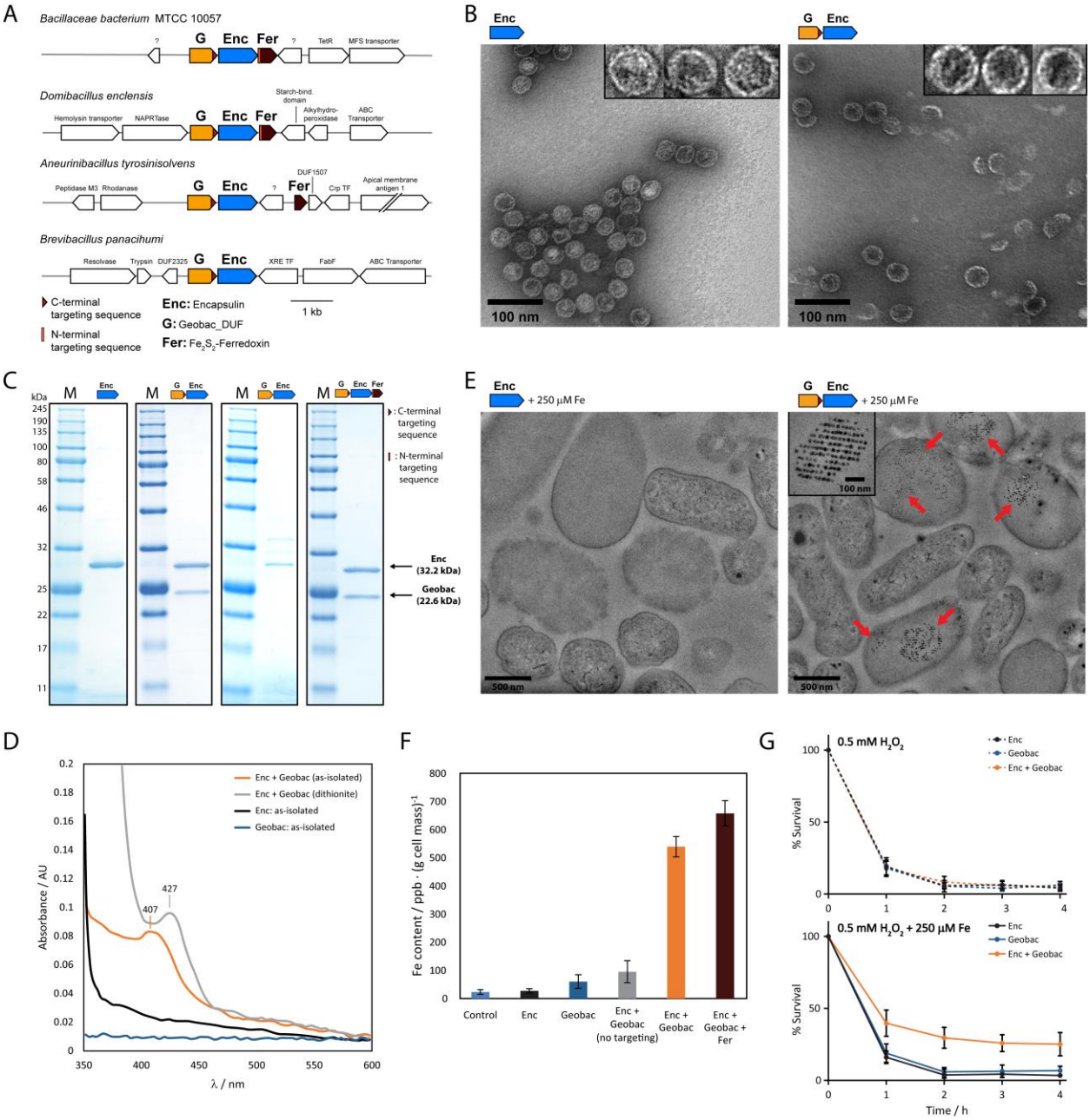

Figure 5: Characterization of the *Bacillaceae bacterium* MTCC 10057 Geobac encapsulin system involved in iron mineralization. (A) Selection of identified Geobac encapsulin gene clusters. (B) Negative-stain TEM micrographs of purified encapsulin particles resulting from *E. coli* cells expressing Enc alone or the Geobac core operon. Insets show magnified particles. (C) SDS-PAGE analysis of purified particles. The expressed gene/operon is shown above the respective gel. (D) UV-Vis analysis of purified

788 Geobac particles and controls. (E) TEM micrographs of fixed *E. coli* cells expressing Enc or Enc+Geobac in
789 the presence of iron sulfate. Intracellular electron-dense particles are indicated by red arrows. The inset
790 shows a magnification of regularly arranged electron-dense particles found in Enc+Geobac-expressing
791 cells. (F) ICP-MS analysis of washed *E. coli* cells expressing different components of the Geobac
792 encapsulin system. Data are represented as mean ± SD of 3 biological replicates. (G) Survival of *E. coli*
793 cells expressing Enc, Geobac or Enc+Geobac in the presence of H_2O_2 (top panel) or H_2O_2 and iron sulfate
794 (lower panel). Data are represented as mean ± SD of 3 biological replicates.

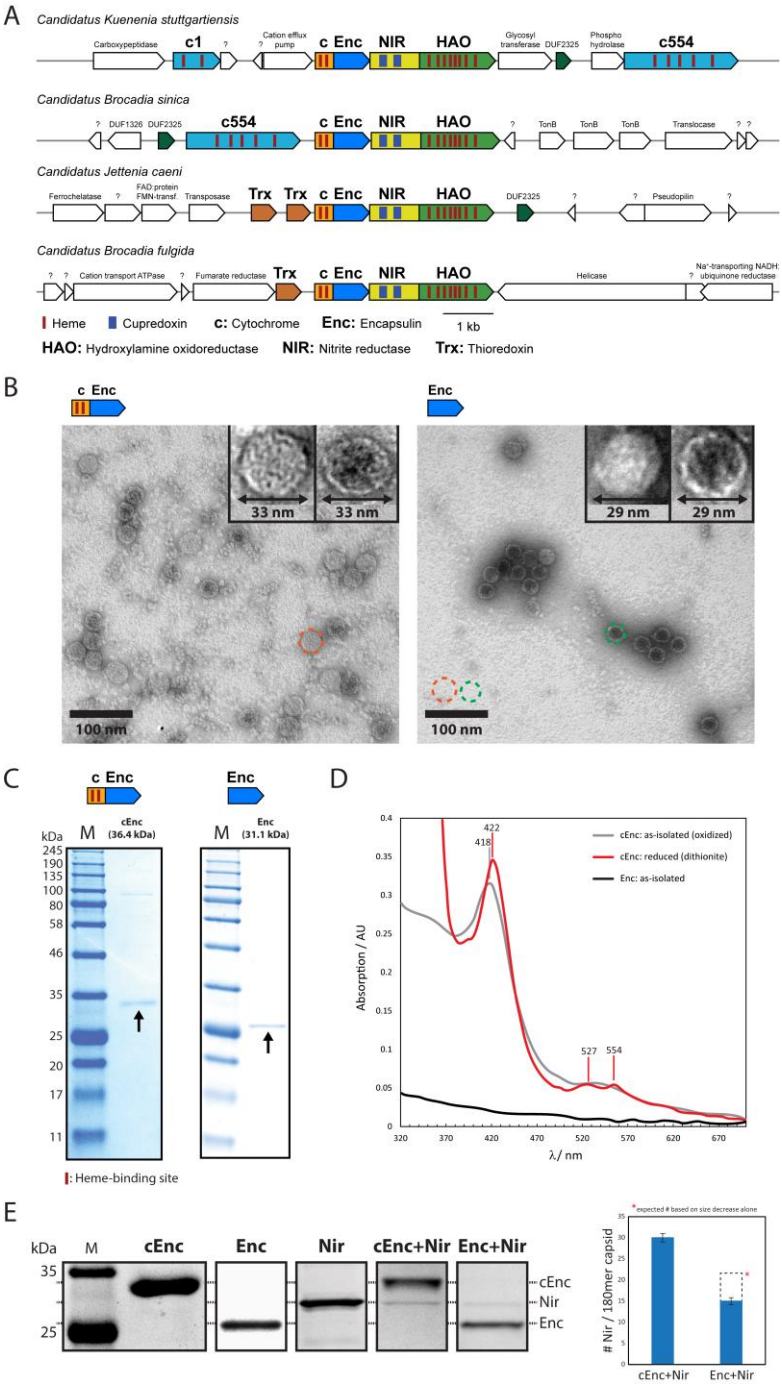

Figure 6: Characterization of the encapsulin system in the anammox bacterium *K. stuttgartiensis*. (A) Encapsulin operons found in 4 anammox bacteria. (B) TEM micrographs of purified *K. stuttgartiensis* encapsulins with (left) or without (right) N-terminal cytochrome fusion domain. Dotted circles are used to illustrate their size difference. (C) SDS-PAGE gels of cEnc and Enc. (D) UV-Vis spectroscopy of cEnc

800 showing the characteristic absorption pattern of c-type cytochromes. (E) SDS-PAGE gels of purified NIR
801 and different particles from *E. coli* expressing different components of the cEnc+NIR-HAO system
802 (indicated above each lane). The panel on the right shows the decrease in NIR loading when the N-
803 terminal cytochrome domain is missing. Data are represented as mean ± SD of 3 separate purifications
804 and gels.